Anatomy of high-uniform unidirectional volatile switching behavior in SiO_2/TiO_2-based selection device

Liping Fu [a], Kuan Yang[b], Xiaoping Gao[c,*], Xiaoqiang Song[a], Zewei Wu[a], Xiaolong Fan[a], and Yingtao Li[a,*]

[a] School of Physical Science and Technology, Lanzhou University,Lanzhou 730000, China

[b] Cuiying Honors College,Lanzhou University, Lanzhou 730000, China

[c] Institute of Sensor Technology, Gansu Academy of Sciences, Lanzhou 730000, P. R. China

Email: ytli@lzu.edu.cn, xp.gao@gsas.ac.cn

Abstract:

Unidirectional volatile switching behavior is a typical resistive switching phenomenon in oxides, which has been proposed as attractive candidates for selection devices for high density memory and neuromorphic systems applications with cross-point arrays. However, the microscopic origin of the underlying mechanism is still unclear due to the lack of direct experimental evidence. Here, a high performance selection device with a low forming voltage, low OFF-state current, high nonlinearity, and excellent uniformity is proposed in SiO_2/TiO_2 stacked structure. The underlying nature of the unidirectional volatile switching behavior in the Pt/Ag/SiO_2/TiO_2/Ti selection device is revealed by using scanning electron microscope and energy-dispersive X-ray spectroscopy analysis in planar structure devices, which can be attributed to the unstable conductive filament (CF) consisting of Ag nanoparticles formed in the SiO_2 layer, and the Schottky contact formed between the Ag CF and TiO_2 interface. This work provides clearly experimental evidence to deepen understanding of the mechanism for unidirectional volatile switching behavior, which can provide a guide to further improve the device performances for high density memory and neuromorphic systems applications.

Keywords: volatile switching, underlying mechanism, selection device, high density memory, neuromorphic system

1. Introduction

Resistive random access memory (RRAM) devices, based on resistive switching characteristics between a high resistance state (HRS) and a low resistance state (LRS) driven by voltage or current bias, have been intensively studied and considered to be promising candidates for both neuromorphic computing [1-6] and next-generation nonvolatile memory applications [7-11] due to their excellent scalability, low power consumption, low cost, high density 3D integration, excellent compatibility with the current complementary metal oxide semiconductor (CMOS) technology [1,7-13], and a close resemblance to the operating characteristics of bio-synapse [1-2,6,15]. These applications typically require a large cross-point array of RRAM devices [16-18]. However, the integration of cross-point array consisting of only RRAM cell suffers unavoidable cross-talk interference due to sneakpath currents through neighboring unselected cells, which severely impede the proper operation of the array [17-22]. To solve the critical issue in cross-point array, numerous access devices with nonlinear response are usually connected to each RRAM cell of the array [23-27].

Recently, two-terminal thin-film based volatile RRAM devices which feature high nonlinearity, fast switching speed, high endurance, short relaxation time, as well as 3D stacking capability [17,22,27-31] have been used as selector devices to suppress crosstalk effect in cross-point arrays [17,22,27,28]. On the other hand, they have also been proposed as attractive candidates in bio-inspired neuromorphic systems as short-term synapses [6,14,29] and integrate-and-fire neurons [30,31]. Although various types of volatile RRAM devices have been developed [27-38], the intrinsic mechanism of the volatile switching behavior is still unclear. Indeed, the intrinsic mechanism is particularly critical for optimizing device structure and improving device performance. Therefore, the revelation of the intrinsic mechanism of volatile switching behavior will provide important guidelines and shed new insights into the resistive switching study of volatile RRAM devices.

Generally, volatile resistive switching behaviors can be classified as two modes: bidirectional volatile switching (BS) [17,22,27,28] with symmetric switching characteristics and unidirectional volatile switching (US) [32] with asymmetric switching characteristics. In the BS mode, the volatile switching behavior has been attributed to the spontaneous rupture of the thin and unstable conductive filament (CF) within the switching layer as the external electrical bias is removed [17,32,33]. In the US mode, although thermally activated drift/diffusion switching models based on Monte Carlo simulations of Ag nanoparticle Brownian-like motion [34], Gibbs–Thomson effect, and interfacial energy minimization [17] have been proposed to quantitatively interpret the asymmetric unidirectional switching phenomenon, a detailed experimental study of the underlying mechanism for this phenomenonis still lacking, especially lacking of direct evidences to uncover why asymmetric unidirectional switching characteristics happen in the US mode.

In this work, we report an asymmetric unidirectional volatile switching selection device in SiO_2/TiO_2 bilayer stacked structure. The fabricated two-terminal Pt/Ag/SiO_2/TiO_2/Ti volatile selection device shows a low forming voltage (~1.5V), high selectivity (>10^6), low OFF-state current (~10pA), and uniform resistive switching. Using scanning electron microscope (SEM) and energy-dispersive X-ray spectroscopy (EDS) analysis, we provide unambiguous evidence to directly reveal the microscopic origin of the unidirectional volatile switching behavior. Obtaining these pieces of information not only help elucidate the underlying nature of the unidirectional volatile switching phenomenon, but guide the design of volatile RRAM devices for cross-point memory arrays and neuromorphic systems applications.

2. **Experimental**

The unidirectional volatile selection devicewith Pt/Ag/SiO_2/TiO_2/Ti vertical structure was directly fabricated on SiO_2/Si substrate. A 65-nm-thick Ti film was first deposited on the SiO_2/Si substrate by electron beam evaporation to form the bottom electrode. Subsequently, a 40-nm-thick TiO_2 film was deposited on the Ti bottom electrode by an atomic layer

deposition (ALD) system at 250 °C substrate temperature. $TiCl_4$ was used as the Ti precursor and H_2O was used as the oxygen precursor. An atomic layer deposition cycle with 4 steps was adopted for this process. The 4 steps were $TiCl_4$ reactant, N_2 purge, H_2O reactant, and N_2 purge, respectively. Then,a 20-nm-thick SiO_2 film was deposited on the TiO_2 film by sputtering. Finaly, 10/35 nm Pt/Ag top electrode (TE) with areas of 100×100 μm^2 was deposited by electron beam evaporation followed by a lift-off photolithographic process. The thin Pt film acts as the part of the protective layer to avoid the oxidation of the Ag TE, and to prevent the probe tip from scratching the device surface during testing. For the Ag/SiO_2/Ti and Ag/TiO_2/Ti planar structure devices, 40-nm-thick SiO_2 and TiO_2 films were prepared on the SiO_2/Si substrate by sputtering and ALD, respectively. After first photolithography, 80-nm-thick Ti layers were deposited on the SiO_2 and TiO_2 films by electron beam evaporation. Then, rectangle Ti electrode with area of 100 μm×5 mm was released using a lift-off process. Subsequently, Ag electrode patterns composed of a 100 μm×100 μm square and a 20 μm×5 μm rectangle tip were generated by photolithography. Subsequently, 80-nm-thick Ag layers were deposited by electron beam evaporation and released by lift-off process. The gap between Ag and Ti electrodes ranges from 200 nm to 2 μm.

The electrical characteristics of all the fabricated devices were performed by using an Agilent B1500A semiconductor deviceanalyzer at room temperature. During the measurements, the bias voltage was applied on the Ag electrode while the Ti electrode was grounded. TEM measurements were performed with a 200 kV high-resolution TEM (HR-TEM, JEOL JEM2100F). The TEM specimens were prepared using a dual-beam focused ion beam (FIB) system (Seiko 4050MS). The elemental distribution was determined by the EDS mapping. The morphology of CF in the device was detected by using a field-emission scanning electron microscopic (Apreo S).

3. Results and discussion

3.1. Structural and electrical properties

The schematic of the device structure is shown in Fig. 1a, and a cross-sectional bright-field transmission electron microscopy (TEM) image and relevant EDS mapping images of our fabricated device with Pt/Ag/SiO_2/TiO_2/Ti stacked structure on SiO_2/Si substrate are shown in Fig. 1b and Fig. 1c, respectively. It is clear that the Pt/Ag/SiO_2/TiO_2/Ti multi-layer films are well stacked on SiO_2/Si substrate with thicknesses of about 10/35/20/40/65 nm, respectively.

The as-deposited fresh devices are normally in the high resistive state (OFF-state), and their initial resistances are about 10^{11} Ω at a 0.3V read voltage. To trigger repeatable resistive switching behavior in the fresh device, an electroforming process (switching the fresh device from the initial OFF-state to the low resistive state (ON-state)) is generally needed [33]. Because of the asymmetric structure of our devices, an electroforming process with positive voltage on the Ag TE is required, and a negative voltage applied to the TE could not lead to the electroforming process. Fig. 2a shows the typical current-voltage (*I*-*V*) curve of the Pt/Ag/SiO_2/TiO_2/Ti device with a high compliance current (I_{comp}) of 1mA. When a I_{comp} of 1mA is applied on the fresh device, a gradual increase of device current can be observed at a low voltage range, while a sudden increase of device current to the I_{comp} at a forming voltage of about 2.35V, and the device switches to a low ON-state. Unfortunately, the ON-state obtained under the I_{comp} of 1 mA cannot be reset to a stable OFF-state again either in positive voltage or negative voltage, meaning that the device may be completely broken down due to the higher forming voltage when a higher I_{comp} is applied [39]. However, it is gratifying to note that repeatable volatile resistive switching characteristics can be obtained when lower I_{comp} are used. Fig. 2b shows the *I*-*V* curves of the Pt/Ag/SiO_2/TiO_2/Ti device with lower I_{comp} values varied from 0.1μA to 100μA. During the negative-voltage sweep, the current is extremely low, and no forming process can be observed, while forming clearly appears for a positive voltage. By sweeping the voltage from zero to a positive voltage, a gradual increase of device current can be observed. The device current reaches to I_{comp} at voltages about 1.5V, and the device switches from the initial OFF-state to ON-state. When the voltage is swept

from 2V back to 0V, the ON-state resistance of the device cannot be maintained and reverts spontaneously to the OFF-state as soon as the applied voltage is close to zero. These results reveal the unidirectional volatile switching behavior in the Pt/Ag/SiO_2/TiO_2/Ti device. More importantly, low leakage current in the pA range and nonlinearity as high as 3×10^6 at the read voltage (V_{READ}=1.5V) and half-read voltage ($1/2V_{READ}$=0.75V) can be achieved by using the I_{comp} of 100μA (Supporting Information Fig. S1).

In order to explore the origin of the volatile switching behavior in the Pt/Ag/SiO_2/TiO_2/Ti device, a kinetic Monte Carlo model was constructed to investigate the microstructure evolution of metal Ag atoms/ions in SiO_2/TiO_2 films. To reflect stochastic nature in migration of Ag atoms/ions which induces instability of Ag conductivefilament (CF), noise function, depicted by a Wiener process with parameters related to appled bias and electrical field, was added to model. The dynamics of the Ag ions are simulated by the following equation:

$$\mathrm{d}u = \nabla \cdot (\mathrm{v}\, n_D - D\, \nabla n_D)\mathrm{d}t + \nabla \cdot D \nabla n_D \mathrm{d}W_t$$

$$\mathrm{d}n_D = -\mathrm{d}u$$

where n_D, u are the concentration and displacement of the Ag ion. D and v are diffusivity and drift velocity, respectively. The calculation of these parameters is the same as [40,41]. The equation is solved by Matlab. To obtain necessary temperature and electrical field profile, FreeFem++ is utilised to solve the Fourier Equation.

Fig. 2c shows the simulated Ag CF microstructure evolution during the forming process in SiO_2/TiO_2 films. It is noted that there are some Ag atoms/ions within SiO_2 film, but there are almost no Ag atoms/ions within TiO_2 film when a votage is supplied. This may be due to that a high Schottkybarrier is formed between Ag and TiO_2interface [42]. The high Schottky barrier between Ag and TiO_2 interface prevents Ag ions from moving forward into the TiO_2 film. More importantly, it can be seen from Fig. 2c (1 to 3) that discontinuous CF channel consisting of discrete Ag nanoparticles with poor continuity is formed within the whole SiO_2 layer when the voltage reaches to 1.5V. However, when the voltage is swept back to 0V, the

discontinuous CF channel is completely disrupted, as shown in Fig. 2c (4 to 6). Then, the device will be back to the OFF-state.

To further evaluate the uniformity of our fabricated selection device, we analyzed the statistical distributions of switching voltages and currents obtained by a direct current (DC) cycling test. Fig. 3 shows the cycle-to-cycle statistical distributions under the I_{comp} of 100μA. As shown in Fig. 3a, the shape of the *I–V* curve is similar to that in the first sweep and only a little voltage and current variations are observed after 10^3 successive DC cycles. The statistical distributions of the current values at 1.5V and 0.75V during 10^3 successive switching cycles are shown in Fig. 3b. As shown in Fig. 3b, only small current variations and high nonlinearity of more than 10^6 are observed. Such a high selectivity could be used to suppress crosstalk effect in the cross-point array. The statistical data of the histograms for the turn-on voltage (V_{ON}) and turn-off voltage (V_{OFF}) are shown in Fig. 3c and Fig. 3d, along with the Gaussian fit of each histogram. Excellent uniformity with a negligible standard deviation is achieved with an ultralow σ value of 0.01 for V_{ON} and 0.02 for V_{OFF} (σ is a parameter of the Gaussian distribution), indicating excellent uniformity is achieved in the Pt/Ag/SiO_2/TiO_2/Ti selection device. Fig. 3e shows the simulated microscopic changes and dynamic evolution process of Ag CF in both ON-state and OFF-state during the first (1st) cycle and the thousandth (1000th) cycle. It is found that the morphology of Ag CF of both states in the 1st cycle is similar to that in the 1000th cycle (image 1 versus image 3, image 2 versus image 4), and only a little variations are observed after 1000 successive switching cycles. Extrapolating from these results, the excellent uniformity of current values and voltage values in the Pt/Ag/SiO_2/TiO_2/Ti selection device can be attributed to the similar morphology of Ag CF in different switching cycles.

3.2. Resistive switching mechanism

In order to further elucidate the original nature of the unidirectional volatile switching characteristics in the Pt/Ag/SiO_2/TiO_2/Ti selection device, we fabricated two control samples

with Ag/TiO_2/Ti and Ag/SiO_2/Ti structures, where the thicknessesof the TiO_2 and SiO_2 layers are the same as those in the Pt/Ag/SiO_2/TiO_2/Ti selection device. The *I–V* curves of the Ag/TiO_2/Ti and Ag/SiO_2/Ti structute devices are shown in Supporting Information Fig. S2 and Fig. S3, respectively. In the case of Ag/TiO_2/Ti structute, the device exhibits nonlinear diode characteristics, as shown in Supporting Information Fig. S2. The rectifying *I–V* characteristic of the Ag/TiO_2/Ti device can be attributed to the Ohmic contact at TiO_2/Ti interface and the Schottky contact at the Ag/TiO_2 interface [18,42]. As for the Ag/SiO_2/Ti structute device, the *I–V* characteristics shown in Supporting Information Fig. S3 are performed under different I_{comp} of 1μA, 10μA, 100μA, and 1mA, respectively. From the *I–V* curves in Supporting Information Fig. S3 and Fig. 1, the Ag/SiO_2/Ti device has the similar initial resistance as the Pt/Ag/SiO_2/TiO_2/Ti selection device (about 10^{11} Ω). Therefore, the bulk resistance of the SiO_2 layer is the main attributer for the Pt/Ag/SiO_2/TiO_2/Ti fresh device. However, different from the unidirectional volatile switching behavior obtained in the Pt/Ag/SiO_2/TiO_2/Ti selection device (Fig. 1), the ON-state of the Ag/SiO_2/Ti device cannot be switched to a stable OFF-state after the forming process even at a very low I_{comp}, as shown in Supporting Information Fig. S3.

There have been numerous studies that have shown the contact of bi-layer film plays an important role and has great influence on the resistive switching characteristics of RRAM devices [43,44]. To further clarify this, we then fabricated another control sample with the Ag/TiO_2/SiO_2/Ti bi-layer structure under the same process. The *I–V* curve of the control Ag/TiO_2/SiO_2/Ti device with I_{comp} of 100μA is shown in Supporting Information Fig. S4. It is worth noting that, different from the Pt/Ag/SiO_2/TiO_2/Ti selection device, volatile switching characteristic cannot be achieved in the Ag/TiO_2/SiO_2/Ti structute device. Thus, it is indicated that the unidirectional volatile switching characteristics in the Pt/Ag/SiO_2/TiO_2/Ti selection device is not resulted from the contact of $SiO_2$and TiO_2.

In recent years, planar structure RRAM devices based on an active electrode (e.g. Ag) and an inert electrode (e.g. Pt or W) are often used to study the underlying mechanism of resistive switching phenomenon due to easy observation on the change of Ag CF between two electrodes [33,45,46]. To further reveal the underlying mechanism of the unidirectional volatile switching behavior in the Pt/Ag/SiO_2/TiO_2/Ti selection device from the microscopic point of view, both SiO_2-based and TiO_2-based planar structure devices were fabricatd. In order to ensure the electroforming operation successfully, an appropriate distance between Ag and Ti electrodes is needed. Thus, the gaps between the Ag and Ti electrodes of the fabricated planar structure devices were designed from 200 nm to 2 μm. The schematic of the planar structure device and typical SEM images of the as-fabricated SiO_2-based planar devices with different gaps are illustrated in Fig. 4a. Fig. 4b shows an as-fabricated SiO_2-based planar device with a gap of 850 nm. As shown in Fig. 4c, the as-fabricated planar device is in the OFF-state with a very low current. In order to trigger the electroforming process and further observe the change of Ag CF in the Ag/SiO_2/Ti planar device, a 40 V constant voltage stress was applied on Ag electrode. As shown in Fig. 4d, the resistance of the planar device suddenly decreased to I_{comp} after 35 s. However, the low resistance state was only maintained for a short time and returned to a high resistance again after 40 s. This result indicates that the CF formed in the Ag/SiO_2/Ti planar structure is unstable during the electroforming process, which leads to a spontaneous rupture. The corresponding SEM image after the electroforming process is shown in Fig. 4e. As can be seen from Fig. 4e, the Ag nanoparticle chain formed between the Ag and Ti electrodes is discontinuous, where a larger number of Ag nanoparticles are generated around Ag electrode and the nanoparticle chain extends towards Ti electrode. On the other hand, the Ag/SiO_2/Ti vertical structure device cannot be switched to a stable OFF-state after the electroforming process, as shown in Supporting Information Fig. S3, which may serve as another clue to claim the unstable CF within the Ag/SiO_2/Ti structure. The chemical compositions of the CF region in the initial-state and after the electroforming

process were analyzed by using EDS analysis for further understanding the nature of the CF. As shown in Fig. 5a, no Ag element signal is found in the initial-state in the SiO_2 film. However, a high Ag element signal was detected in the CF region (e.g. circular region labeled by "1" and "2") after the electroforming process, as shown in Fig. 5b and Fig. 5c. The corresponding EDS elemental mapping images also confirmed that Ag element was present in region 1 and 2, as shown in Supporting Information Fig. S5. In addition, line profile analysis (Fig. 5d) along the red line from region 1 to region 3 in Fig. 4e, again revealing clear Ag element signal along the CF region. These results clearly indicate that Ag is the primary elemental component of the CF in the Ag/SiO_2/Ti device, which is consistent with the previous results obtained by SEM and in situ TEM [33,45].

Fig. 6a shows an as-fabricated TiO_2-based planar device with a gap of about 1 μm. To explore electrical properties of the TiO_2-based planar device, a first negative-voltage sweep (0V → -3V) followed by a positive-voltage sweep (0V → 10V) is applied on Ag electrode to program the fresh device. It is worth noting that the Ag/TiO_2/Ti planar device exhibits rectifying *I-V* characteristic, as shown in Fig. 6b, which is similar to the asymmetric *I-V* characteristic observed in vertical structure device (Supporting Information Fig. S2). Compared with the SEM image of initial-state (before programming) shown in Fig. 6a, the SEM image observed after programming process reveals that no significant change is observed in the region between the two electrodes, as shown in Fig. 6c. On the other hand, the chemical compositions of the interelectrode region before and after programming were analyzed by EDS, as shown in Fig. 6d. It can be seen from Fig. 6d that the element signals are almost the same, and no Ag element signal is detected in the interelectrode region after programming. These results prove that it is difficult for Ag ions to migrate onto TiO_2 film.

Based on the experimental results obtained above, it is clear that unstable Ag nanoparticles based CF is formed in Ag/SiO_2/Ti structure device, movement of Ag ions in TiO_2 film is difficult, and rectifying *I–V* characteristic is observed in Ag/TiO_2/Ti structure device because

of the Schottky contact at the Ag/TiO_2 interface. Therefore, the intrinsic mechanism of the unidirectional volatile switching behavior in our fabricated $Pt/Ag/SiO_2/TiO_2/Ti$ selection device can be schematically summarized in Supporting Information Fig. S6. When a positive voltage is applied on the Ag electrode, Ag ions are generated and will migrate onto the Ti cathode. Because the migration of Ag ions in TiO_2 film is difficult, unstable CF consisting of Ag nanoparticles is only able to form in the SiO_2 layer rather than complete CF between the two electrodes, as illustrated in the ON-state of the Supporting Information Fig. S6. Once the Ag CF formed between the Ag electrode and SiO_2/TiO_2 interface, a Schottky contact is thus formed between the Ag CF and TiO_2 interface, leading to the rectifying *I–V* characteristic of the $Pt/Ag/SiO_2/TiO_2/Ti$ selection device. When the voltage is swept back to 0V, the CF is completely disrupted due to the discontinuous CF channel consisting of discrete Ag nanoparticles, as illustrated in the OFF-state of the Supporting Information Fig. S6.

4. Conclusions

In summary, an asymmetric unidirectional volatile switching selection device with $Pt/Ag/SiO_2/TiO_2/Ti$ structure was presented. Outstanding features such as a low forming voltage, low OFF-state current, high nonlinearity, and excellent uniformity were achieved. Furthermore, the underlying mechanism of the unidirectional volatile switching behavior in the $Pt/Ag/SiO_2/TiO_2/Ti$ selection device was revealed by simulation and experiments. The simulated analysis and SEM results from the planar structure devices directly prove that unstable CF consisting of Ag nanoparticles is only formed in the SiO_2 layer, and then a Schottky contact between the Ag CF and TiO_2 interface begins to appear, leading to the unidirectional volatile switching with rectifying *I–V* characteristic in the $Pt/Ag/SiO_2/TiO_2/Ti$ selection device. The underlying nature of the unidirectional volatile switching behavior illustrated in this work will provide a guide to further improve the device performances for numerous applications, such as high density memory and bio-inspired neuromorphic systems.

Supporting Information

Supporting Information is available from the author.

Acknowledgements

This work is founded by the National Key Research and Development Program of China (Grant No. 2017YFB0405600), the National Natural Science Foundation of China (Grant Nos. 61774079), the Science and Technology Plan of Gansu Province (No. 20JR5RA307), the Key Research and Development Program of Gansu Province (Grant No. 20YF8GA125), the Key Talent Project of Organization Department in Gansu Province, and the Cooperative Project of Gansu Academy of Sciences (Grant No. 2020HZ-2).

References

[1] Yang,J. J.; Strukov, D. B.; Stewart, D. R.*Nat. Nanotechnol.***2013**, 8, 13.

[2] Tang, J. S.; Yuan, F.; Shen, X. K.; Wang, Z. R.; Rao, M. Y.; He, Y. Y.; Sun, Y. H.; Li, X. Y.; Zhang, W. B.; Li, Y. J.; Gao, B.; Qian, H.; Bi, G. Q.; Song, S.; Yang, J. J.; Wu, H. Q.*Adv. Mater.***2019**, 31, 1902761.

[3] Jo, S. H.; Chang, T.; Ebong, I.; Bhadviya, B. B.; Mazumder, P.; Lu, W.*Nano Lett.***2010**, 10, 1297.

[4] Zhang, X. M.; Liu, S.; Zhao, X. L.; Wu, F, C.; Wu, Q. T.; Wang, W.; Cao, R. R.; Fang, Y. L.; Lv, H. L.; Long, S. B.; Liu, Q.; Liu, M.*IEEE Electron Device Lett.*, **2017**, 38, 1208.

[5] Wang, I. T.; Lin, Y. C.; Wang, Y. F.; Hsu, C. W.; Hou, T. H. *IEEE IEDM Tech. Dig.***2014**, 665.

[6] Ohno, T.; Hasegawa, T.; Tsuruoka, T.; Terabe, K.; Gimzewski, J. K.; Aono, M. *Nat. Mater.* **2011**, *10*, 591.

[7] Waser, R.; Dittmann, R.; Staikov, G.; Szot, K.*Adv. Mater.***2009**, 21, 2632.

[8] Kwon, D. H.; Kim, K. M.; Jang, J. H.; Jeon, J. M.; Lee, M. H.; Kim, G. H.; Li, X. S.; Park, G. S.; Lee, B.; Han, S.; Kim, M.; Hwang, C. S. *Nat. Nanotechnol.* **2010**, *5*, 148.

[9] Cavallini, M.; Hemmatian, Z.; Riminucci, A.; Prezioso, M.; Morandi, V.; Murgia, M. *Adv. Mater.***2012**, 24, 1197.

[10] Liu, Q.; Sun, J.; Lv, H.; Long, S.; Yin, K.; Wan, N.; Li, Y.; Sun, L.; Liu, M.*Adv. Mater.* **2012**, 24, 1844.

[11] Seok, J. Y.; Song, S. J.; Yoon, J. H.; Yoon, K. J.; Park, T. H.; Kwon, D. E.; Lim, H.;Kim, G. H.; Jeong, D. S.; Hwang, C. S. *Adv. Funct. Mater.* **2014**, *24*, 5316.

[12] Yang, J. J.; Pickett, M. D.; Li, X.; Ohlberg, D. A. A.; Stewart, D. R.; Williams, R. S. *Nat. Nanotechnol.***2008**, 3, 429.

[13] Liu, Q.; Long, S.; Lv, H.; Wang, W.; Niu, J.; Huo, Z.; Chen, J.; Liu, M.*ACS Nano***2010**,

4, 6162.

[14] Wang, Z.; Joshi, S.; Savel'ev, S. E.; Jiang, H.; Midya, R.; Lin, P.; Hu, M.; Ge, N.; Strachan, J. P.; Li, Z.; Wu, Q.; Barnell, M.; Li, G.-L.; Xin, H. L.; Williams, R. S.; Xia, Q.; Yang, J. J. *Nature Mater.***2016**, 16, 101.

[15] Park, J.; Kwak, M.; Moon, K.; Woo, J.; Lee, D.; Hwang, H. *IEEE Electron Device Lett.*, **2016**, 37, 1559.

[16] Webb, R. C.; Bonifas, A. P.; Behnaz, A.; Zhang, Y.; Yu, K. J.; Cheng, H.; Shi, M.; Bian, Z.; Liu, Z.; Kim, Y. S.; Yeo, W. H.; Park, J. S.; Song, J.; Li, Y.; Huang, Y.; Gorbach, A. M.; Rogers, J. A. *Nat. Mater.* **2013**, *12*, 938

[17] Midya, R.; Wang, Z.; Zhang, J.; Savel'ev, S. E.; Li, C.; Rao, M.; Jang, M. H.; Joshi, S.; Jiang, H.; Lin, P.; Norris, K.; Ge, N.; Wu, Q.; Barnell, M.; Li, Z.; Xin, H. L.; Williams, R. S.; Xia, Q.; Yang, J. J.;*Adv. Mater.* **2017**, *29*, 1604457.

[18] Li, Y. T.; Lv, H. B.; Liu, Q.; Long, S. B.; Wang, M.; Xie, H. W.; Zhang, K. W.; Huo, Z. L.; Liu, M. *Nanoscale***2013**, 5, 4785.

[19] Cho, B.; Kim, T. W.; Song, S.; Ji, Y.; Jo, M.; Hwang, H.; Jung, G. Y.; Lee, T. *Adv. Mater.***2010**, 22, 1228.

[20] Kim, G. H.; Lee, J. H.; Ahn, Y.; Jeon, W.; Song, S. J.; Seok, J. Y.; Yoon, J. H.; Yoon, K. J.; Park, T. J.; Hwang, C. S. *Adv. Funct. Mater.* **2013**, *23*, 1440.

[21] Kim, S.; Zhou, J.; Lu, W. D. *IEEE Trans. Electron Devices* **2014**, *61*, 2820

[22] Wang, M.; Wang, W.; Leow, W. R.; Wan, C. J.; Chen, G.; Zeng, Y.; Yu, J. C.; Liu, Y. Q.; Cai, P. Q.; Wang, H.; Ielmini, D.; Chen, X. D.*Adv. Mater.* 2018, 30, 1802516.

[23] Lee, M. J.; Kim, S. I.; Lee, C. B.; Yin, H.; Ahn, S. E.; Kang, B. S.; Kim, K. H.; Park, J. C.; Kim, C. J.; Song, I.; Kim, S. W.; Stefanovich, G.; Lee, J. H.; Chung, S. J.; Kim, Y. H.; Park, Y. *Adv. Funct. Mater.* **2009**, 19, 1587

[24] Seo, J. W.; Baik, S. J.; Kang, S. J.; Hong, Y. H.; Yang, J. H.; Lim, K. S. *Appl. Phys. Lett.***2011**, 98, 233505.

[25] Kim, G. H.; Lee, J. H.; Ahn, Y.; Jeon, W.; Song, S. J.; Seok, J. Y.; Yoon, J. H.; Yoon, K. J.; Park, T. J.; Hwang, C. S. *Adv. Funct. Mater.* **2013**, *23*, 1440.

[26] Lee, M. J.; Lee, D.; Cho, S. H.; Hur, J. H.; Lee,S. M.; Seo, D. H.; Kim, D. S.; Yang, M. S.; Lee, S.; Hwang, E.; Uddin, M. R.; Kim, H.; Chung, U. I.; Park, Y.; Yoo, I. K. *Nat. Commun.* **2013**, *4*, 2629.

[27] Luo, Q.; Xu, X.; Liu, H.; Lv, H.; Gong, T.; Long, S.; Liu, Q.; Sun, H.; Banerjee, W.; Li, L.; Lu, N.; Liu, M.; *IEEE IEDM Tech. Dig.***2015**, 253-256.

[28] Song, J.; Woo, J.; Prakash, A.; Lee, D.; Hwang, H.;*IEEE Electron Device Lett.*, 2015, 36, 681.

[29] Covi, E.; Lin, Y. H.; Wang, W.; Stecconi, T.; Milo, V.; Bricalli, A.; Ambrosi, E.; Pedretti, G.; Tseng, T. Y.; Ielmini, D. *IEEE ICECS***2019**, 903.

[30] Wang, Z.; Joshi, S.; Savel'ev, S.; Song, W.; Midya, R.; Li, Y.; Rao, M.; Yan, P.; Asapu, S.; Zhuo, Y.; Jiang, H.; Lin, P.; Li, C.; Yoon, J. H.; Upadhyay, N. K.; Zhang, J.; Hu, M.; Strachan, J. P.; Barnell, M.; Wu, Q.; Wu, H.; Williams, R. S.; Xia, Q.; Yang, J. J. *Nature Electronics* **2018**, 1, 137.

[31] Toliar, P.; nchant, J.; Corraze, B.; Janod, E.; Besland, M. P.; Tesler, F.; Rozenberg, M.; Cario, L. *Adv. Funct. Mater.* **2017**, *27*, 1604740.

[32] Wang, Z.; Joshi, S.; Saveliev, S. E.; Jiang, H.; Midya, R.; Lin, P.; Hu, M.; Ge, N.; Strachan, J. P.; Li, Z.; Wu, Q.; Barnell, M.; Li, G. L.; Xin, H. L.; Williams, R. S.; Xia, Q.; Yang, J. J. *Nat. Mater.* **2016**, *16*, 101.

[33] Sun, H.; Liu, Q.; Li, C.; Long, S.; Lv, H.; Bi, C.; Huo, Z.; Li, L.; Liu, M.*Adv. Funct. Mater.* **2014**, *24*, 5679.

[34] Wang, W.; Laudato, M.; Ambrosi, E.; Bricalli, A.; Covi, E.; Lin, Y. H.; Ielmini, D. *IEEE Trans. Electron Devices*. **2019**, 6, 3802.

[35] Dongale, T. D.; Kamble, G. U.; Kang, D. Y.; Kundale, S. S.; An, H. M.; Kim, T. G. *Phys. Status Solidi RRL* **2021,** 15, 2100199.

[36] Jeon, D. S.; Dongale, T. D.; Kim, T. G. *J. Alloy. Compd.* **2021,** 884, 161041.

[37] Yu, M. J.; Son, K. R.; Khot, A. C.; Kang, D. Y.; Sung, J. H.; Jang, I. G.; Y. D.; Dange, Dongale, T. D.; Kim, T. G. *J. Mater. Res. Technol.* **2021,** 15, 1984.

[38] Kim D.; Park, J. H.; Jeon, D. S.; Dongale, T. D.; Kim, T. G. *J. Alloy. Compd.* **2021,** 854, 157261.

[39] Qi, J.; Zhang, Q.; Huang, J.; Ren, J. J.; Olmedo, M.; Liu, J. L. *IEEE Electron Device Lett.* **2011**, 32, 1445.

[40] Bousoulas, P.; Giannopoulos, I.; Asenov, P.; Karageorgiou, I.; Tsoukalas, D. *J. Appl. Phys.* **2017**, 121, 094501.

[41] Larentis, S.; Nardi, F.; Balatti, S.; Gilmer, D. C.; Ielmini, D.; *IEEE Trans. On Electron Devices* **2012**, 59, 9.

[42] Li, Y. T.; Gong, Q. C.; Jiang, X. Y. *Appl. Phys. Lett.***2014**, 104, 132105.

[43] Wu, H. Q.; Li, X. Y.; Wu, M. H.; Huang, F. Y.; Yu, Z. P.;Qian, H.;*IEEE Electron Device Lett.* **2014**, 35, 39.

[44] Lv, H. B.; Li, Y. T.; Liu, Q.; Long, S. B.; Li, L.; Liu, M. *IEEE Electron Device Lett.* **2013**, 34, 229.

[45] Yang, Y. C.; Gao, P.; Gaba, S.; Chang, T.; Pan, X.; Lu, W. *Nat. Commun.***2012**,*3*, 732.

[46] Sun, H.; Lv, H.; Liu, Q.; Long, S.; Wang, M.; Xie, H.; Liu, X.; Yang, X.; Niu, J.; Liu, M. *IEEE Electron Device Lett.* **2013**, *34*, 873 .

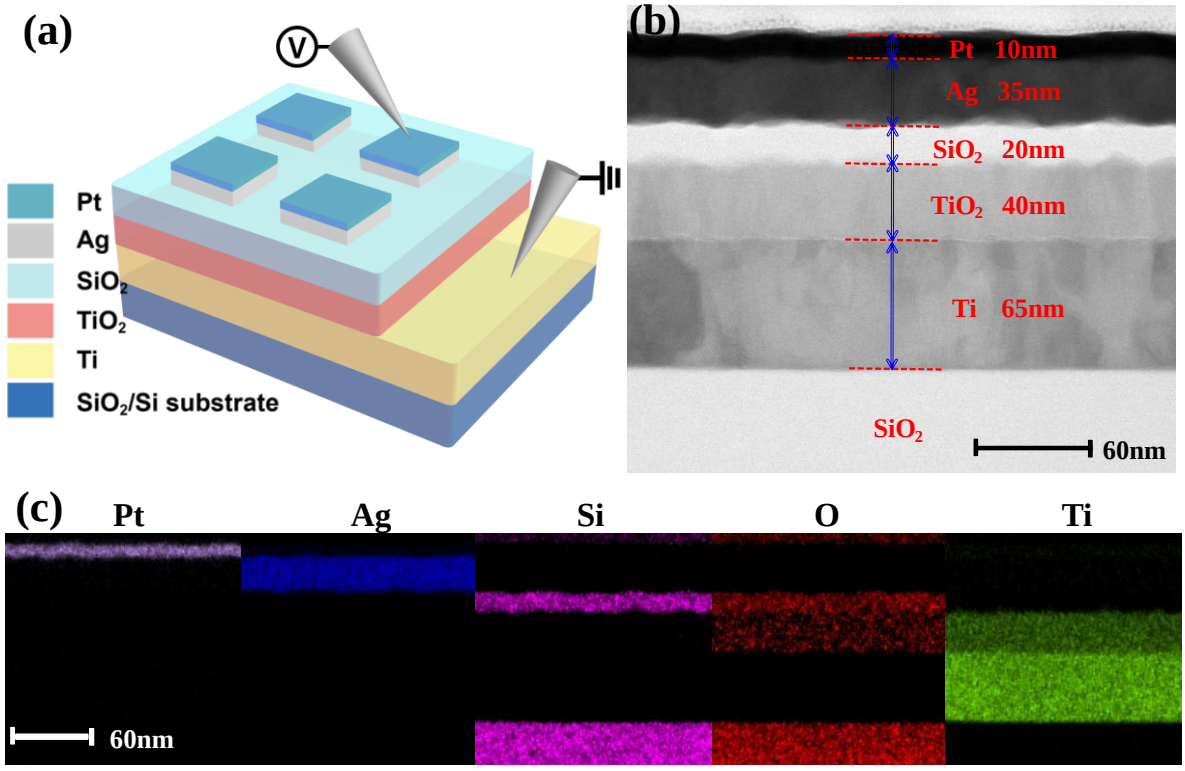

Fig. 1. (a) Schematic of the unidirectional volatile selection device with two-terminal Pt/Ag/SiO_2/TiO_2/Ti stacked structure. (b) A cross-sectional bright-field TEM image of the unidirectional volatile selection device with Pt/Ag/SiO_2/TiO_2/Ti stacked structure on SiO_2/Si substrate. (c) EDS mapping images corresponding to the TEM image.

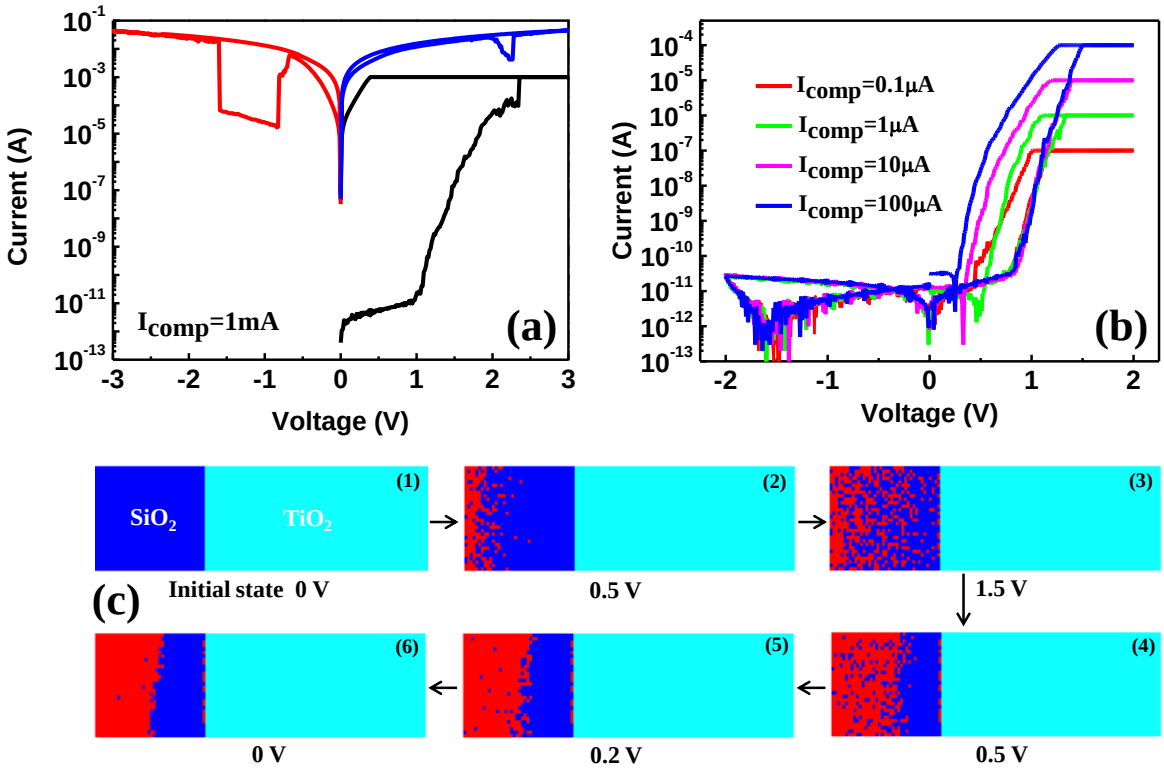

Fig. 2. (a) *I-V* characteristic of the Pt/Ag/SiO_2/TiO_2/Ti device under a high compliance current of of 1 mA. No stable resistive switching characteristic could be obsered in the device with a higher I_{comp} of 1 mA during the electroforming process. (b) Typical *I–V* curves of the Pt/Ag/SiO_2/TiO_2/Ti device under different compliance current of 0.1μA, 1μA, 10μA, and 100μA. Unidirectional volatile switching behaviors were observed when different compliance currents from 0.1μA to 100μA were used during the electroforming process with positive voltage. (c) Simulated dynamic microstructure evolution of Ag CF in SiO_2/TiO_2 films.

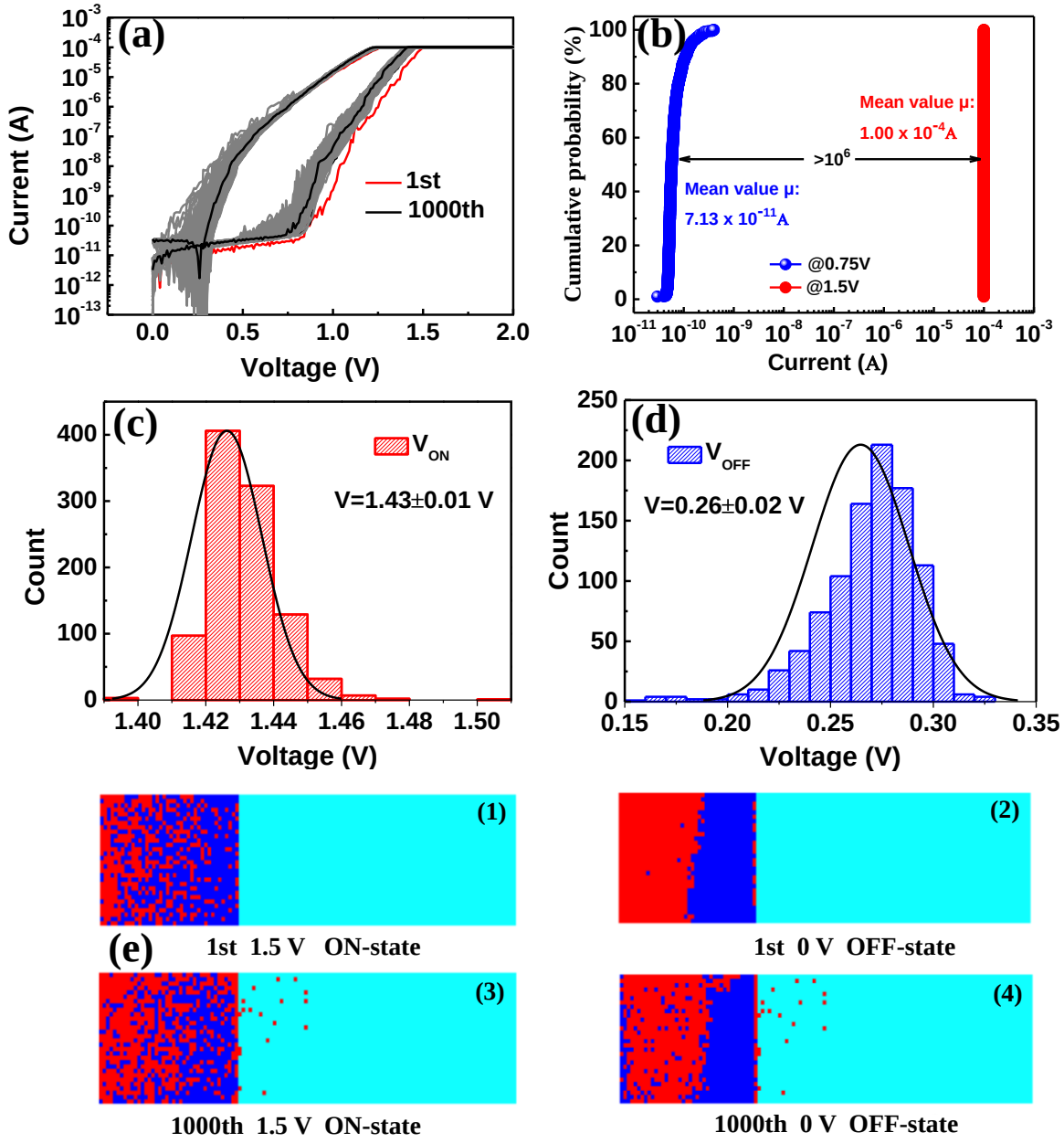

Fig. 3. (a) Reproducibility of the unidirectional volatile switching characteristics of the device under the I_{comp} of 100 μA. After 10^3 successive DC switching cycles, only small voltage and current variations were observed, indicating good reproducible behavior of the device. (b) Statistical distributions of the current at 1.5V and 0.75V for 10^3 successive switching cycles. High selectivity of more than 10^6 could be obtained. (c) Statistical distributions of turn-on voltage (V_{ON}). (d) Statistical distributions of turn-off voltage (V_{OFF}). (e) Simulated microscopic changes of Ag CF of both ON-state and OFF-state in the 1st cycle and the 1000th cycle.

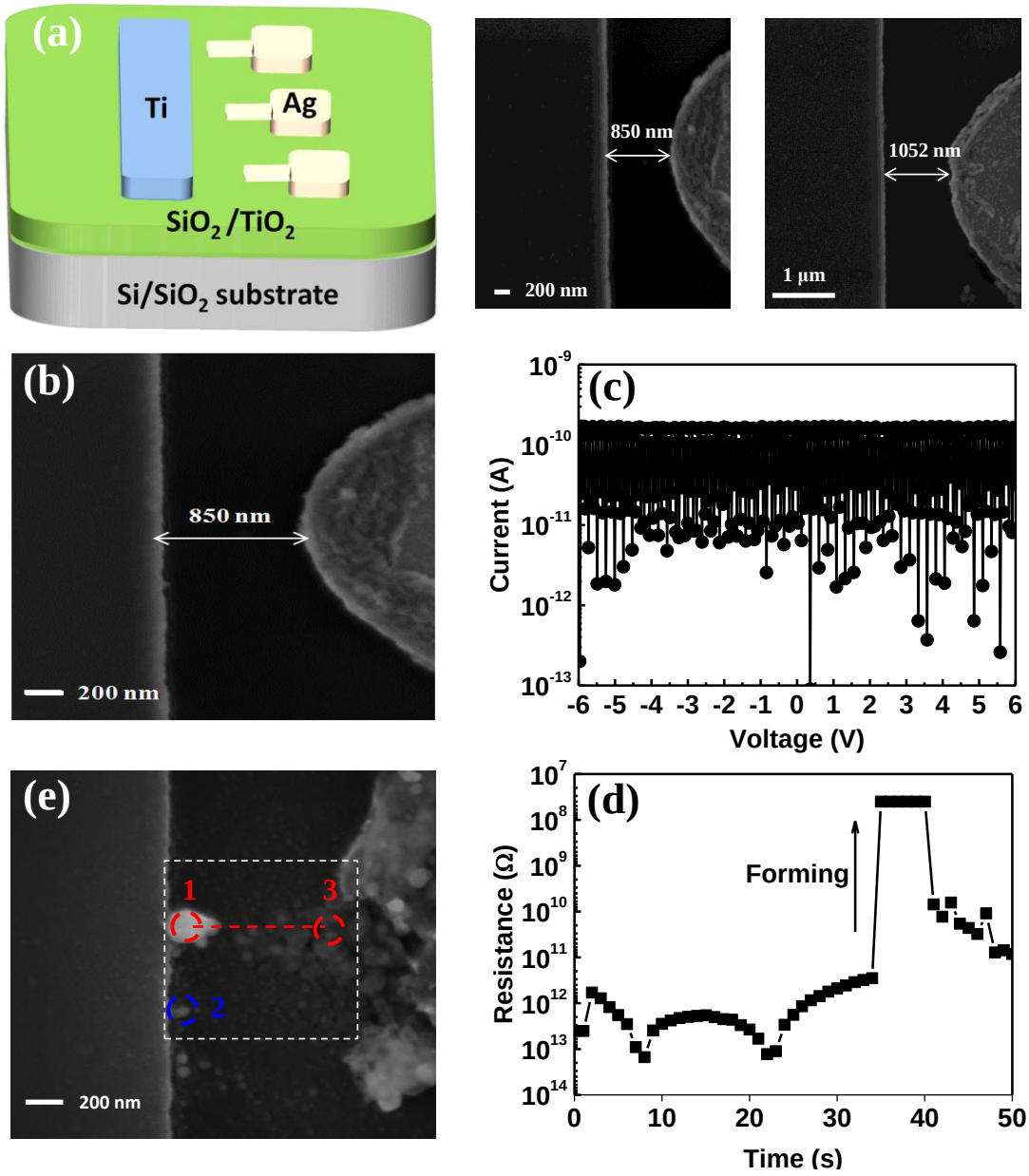

Fig. 4. (a) Schematic and SEM images of the planar device with different gap size. (b) As-fabricated $Ag/SiO_2/Ti$ planar device with a gap of 850 nm without any electrical treatment. (c) Typical *I–V* curve of the as-fabricated $Ag/SiO_2/Ti$ planar device. (d) Resistance-time curve of the $Ag/SiO_2/Ti$ planar device under a 40 V constant voltage stress. (e) SEM image capturing the CF morphology in the $Ag/SiO_2/Ti$ planar device after a 40 V constant voltage stress. The CF consisting of Ag nanoparticles between the Ag and Ti electrodes is discontinuous.

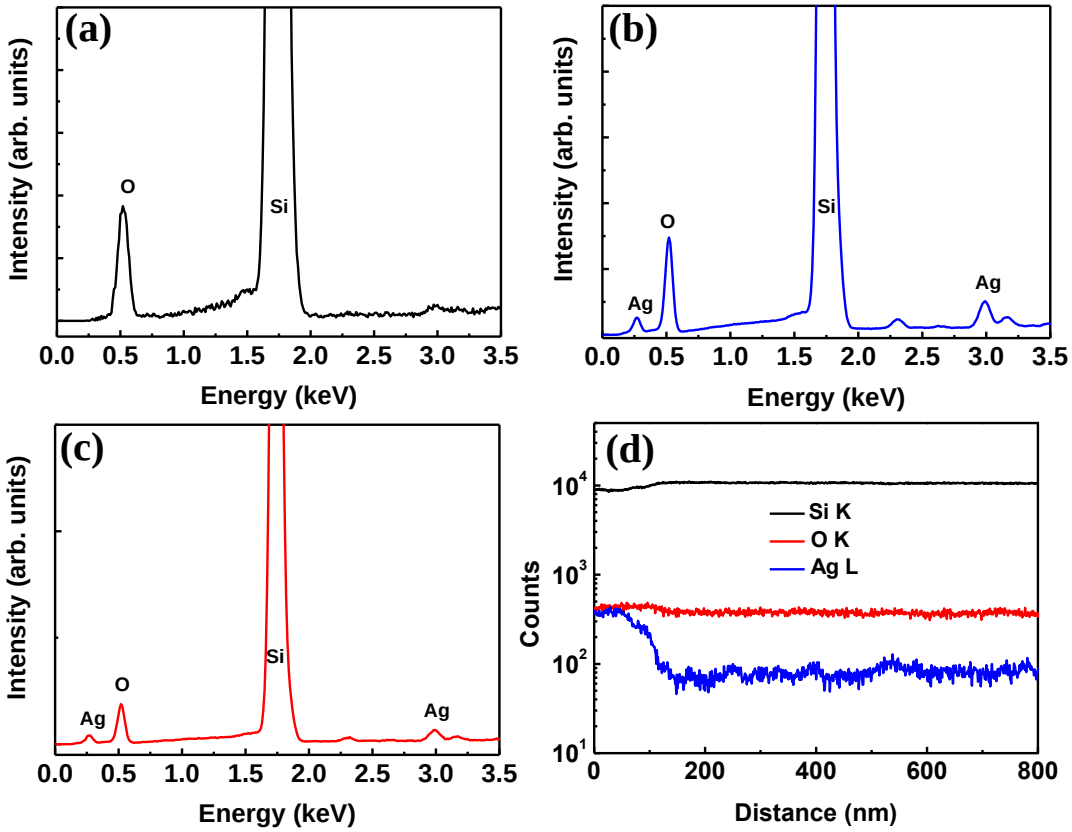

Fig. 5. EDS spectrums of the Ag/SiO_2/Ti planar device tested in initial-state (a) and at circular region labeled by "1" (b) and "2" (c) in the Fig. 4e. The EDS spectrums after a 40 V constant voltage stress were obtained in the CF region whereas initial-state was obtained in the SiO_2 film. Compared to the initial-state without Ag element signal, Ag element signal is obviously observed in the CF region. (d) EDS line profile analysis along the red line from "1" to "3" in the Fig. 4e.

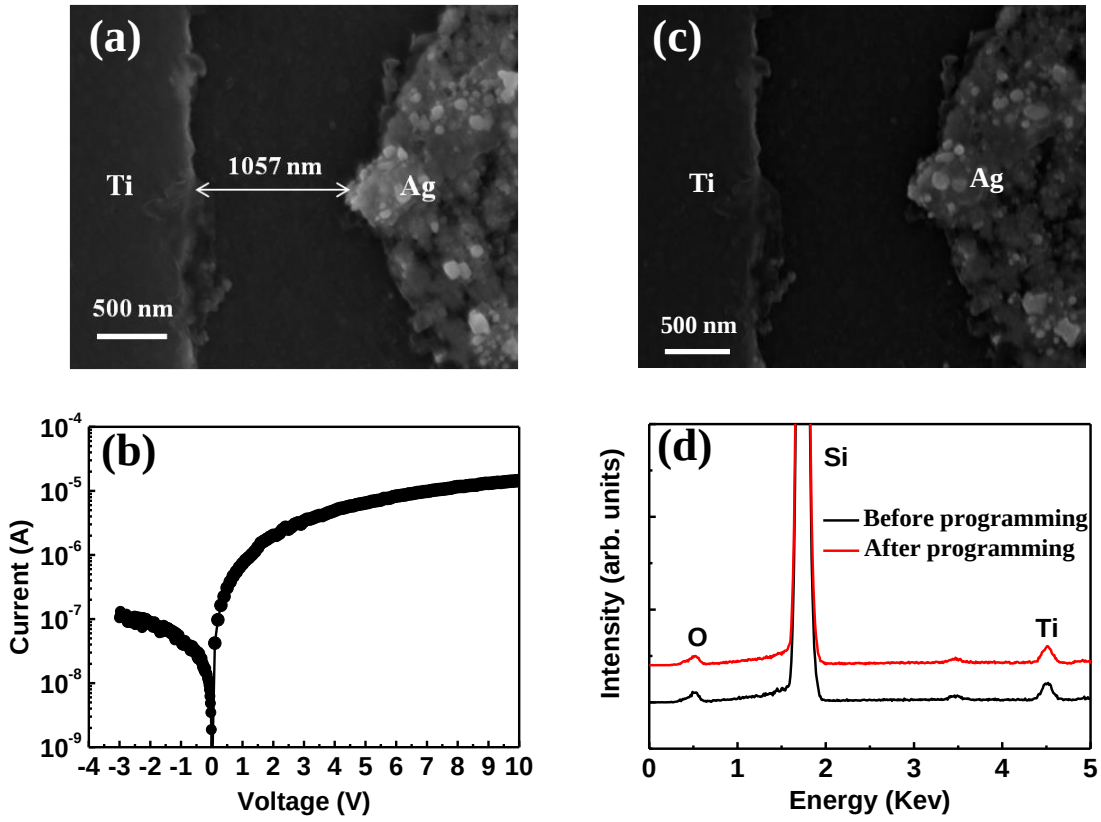

Fig. 6. (a) SEM image of the Ag/TiO_2/Tiplanar devicebeforeprogramming. (b) *I*–*V*curve of the Ag/TiO_2/Tiplanar device by using a first negative-voltage sweep (0V→ -3V) followedby a positive-voltage sweep (0V→ 10V). (c) SEM image of the Ag/TiO_2/Tiplanar deviceafterprogramming. No significant change is observed beforeand after programming. (d) EDS spectrums of the Ag/TiO_2/Tiplanar device testedbeforeand after programming.

Supporting Information

Anatomy of high-uniform unidirectional volatile switching behavior in SiO_2/TiO_2-based selection device

Liping Fu [a], Kuan Yang[b], Xiaoping Gao[c,*], Xiaoqiang Song[a], Zewei Wu[a], Xiaolong Fan[a], and Yingtao Li[a,*]

[a] School of Physical Science and Technology, Lanzhou University,Lanzhou 730000, China

[b] Cuiying Honors College,Lanzhou University,Lanzhou 730000, China

[c] Institute of Sensor Technology, Gansu Academy of Sciences, Lanzhou 730000, P. R. China

Email: ytli@lzu.edu.cn, xp.gao@gsas.ac.cn

Keywords: volatile switching, underlying mechanism, selection device, high density memory, neuromorphic system

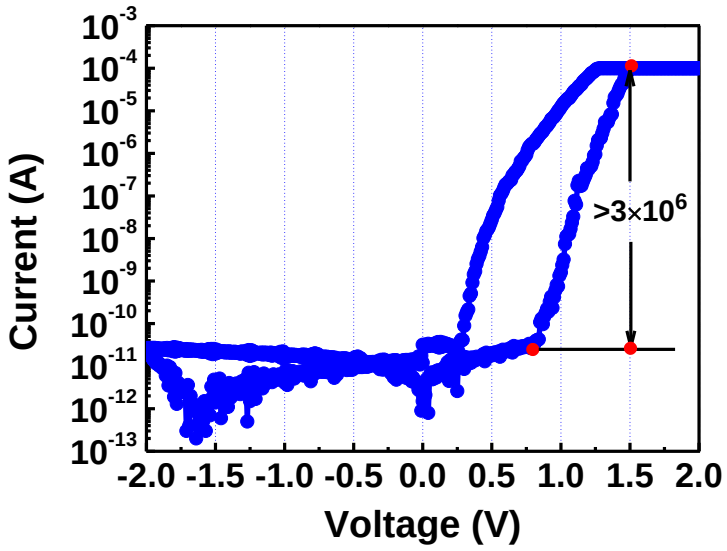

Fig. S1. *I-V* curve of the Pt/Ag/SiO_2/TiO_2/Ti device with a compliance current of 100μA. A high selectivity of more than 3×10^6 at the read voltage (V_{READ}=1.5V) and half-read voltage ($1/2V_{READ}$=0.75V) is obtained.

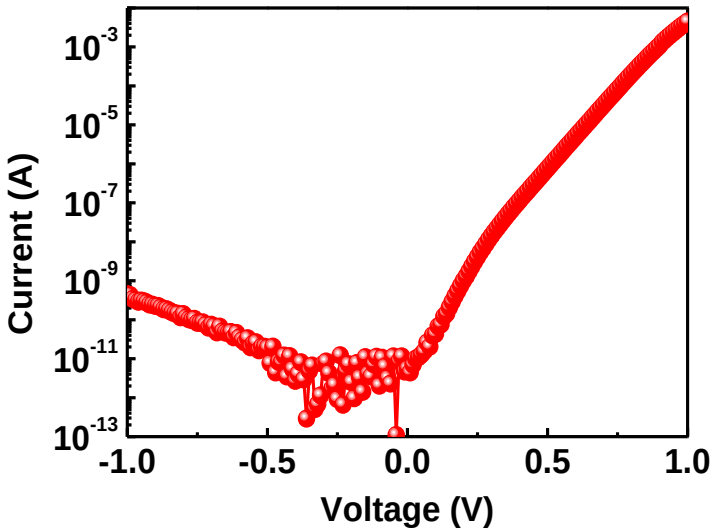

Fig. S2. *I–V* curve of the Ag/TiO_2/Ti device with obvious rectifying characteristic.

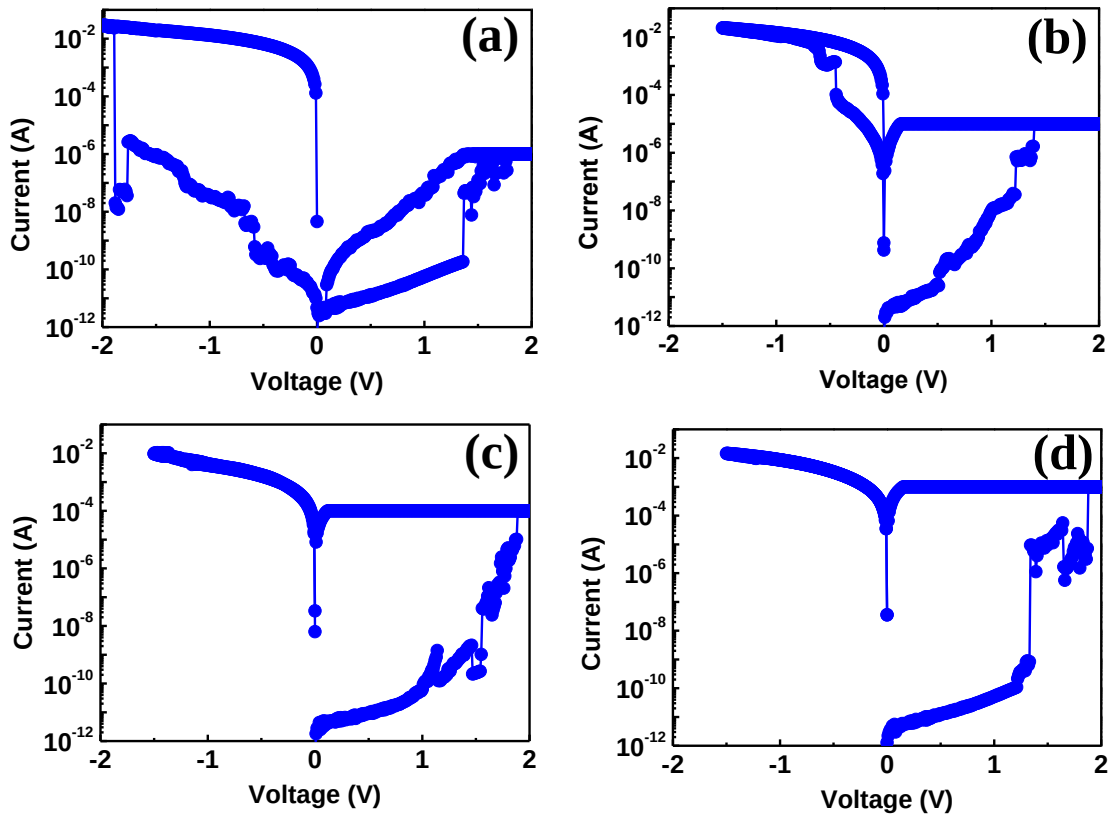

Fig. S3. Typical *I–V* curves of the Ag/SiO_2/Ti device under different compliance current of (a) 1 µA, (b) 10 µA,(c) 100 µA, and (d) 1mA, respectively. The ON-state of the device cannot be switched to a stable OFF-state after the forming process.

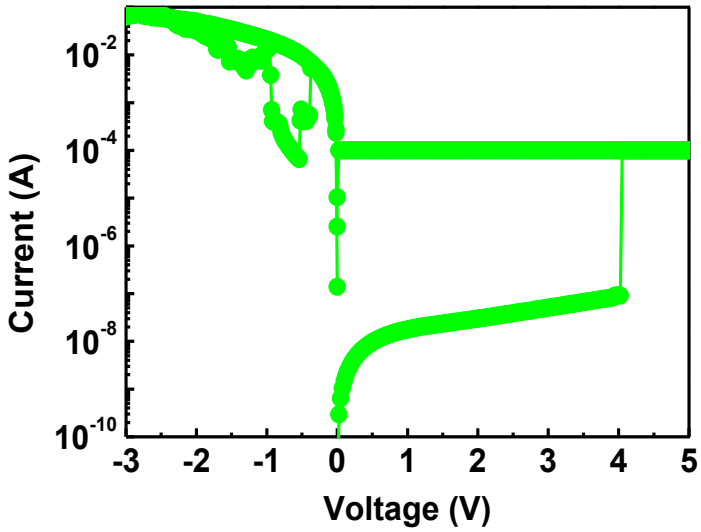

Fig. S4. *I–V* curve of the control Ag/TiO_2/SiO_2/Ti device.

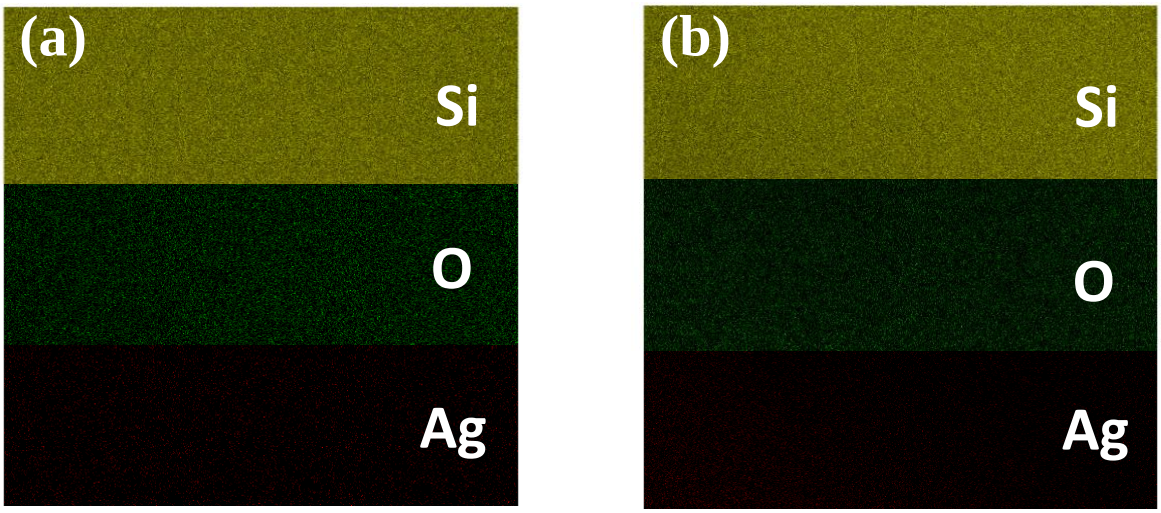

Fig. S5. EDS mapping images of Si, O and Ag elements, respectively, corresponding to the circular region labeled by "1"(a) and "2" (b) in the Figure 4e. Ag element signal is obviously observed in region "1" and "2", indicating that Ag is the primary elemental component of the CF.

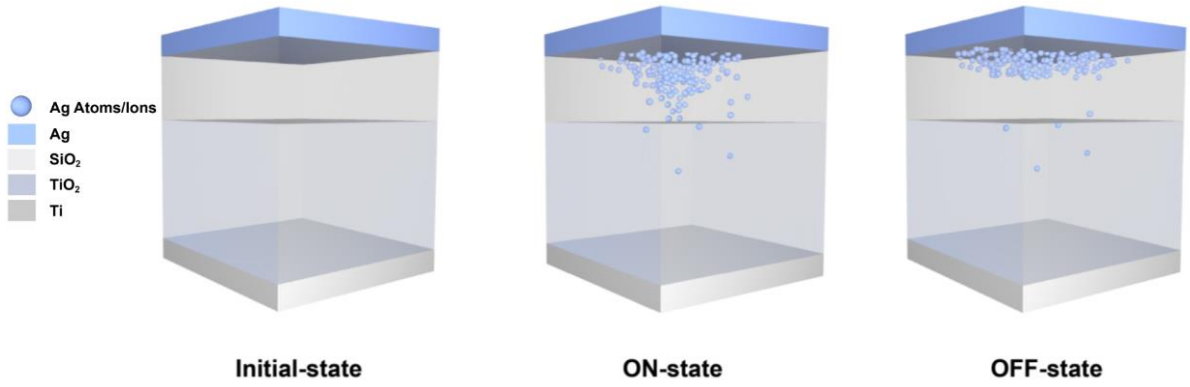

Fig. S6. Schematic illustration of the unidirectional volatile switching behavior in the Pt/Ag/SiO_2/TiO_2/Ti selection device.